CrystEngComm

PAPER

View Article Online
View Journal | View Issue

Check for updates

Cite this: *CrystEngComm*, 2024, **26**, 1219

An unusual ionic cocrystal of ponatinib hydrochloride: characterization by single-crystal X-ray diffraction and ultra-high field NMR spectroscopy†

Alexander J. Stirk, ‡[a] Sean T. Holmes, ‡[bc] Fabio E. S. Souza,[a] Ivan Hung,[c] Zhehong Gan,[c] James F. Britten,[d] Allan W. Rey[a] and Robert W. Schurko *[bc]

This study describes the discovery of a unique ionic cocrystal of the active pharmaceutical ingredient (API) ponatinib hydrochloride (**pon·HCl**), and characterization using single-crystal X-ray diffraction (SCXRD) and solid-state NMR (SSNMR) spectroscopy. **Pon·HCl** is a multicomponent crystal that features an unusual stoichiometry, with an asymmetric unit containing both monocations and dications of the ponatinib molecule, three water molecules, and three chloride ions. Structural features include (i) a charged imidazopyridazine moiety that forms a hydrogen bond between the ponatinib monocations and dications and (ii) a chloride ion that does not feature hydrogen bonds involving any organic moiety, instead being situated in a "square" arrangement with three water molecules. Multinuclear SSNMR, featuring high and ultra-high fields up to 35.2 T, provides the groundwork for structural interpretation of complex multicomponent crystals in the absence of diffraction data. A ^{13}C CP/MAS spectrum confirms the presence of two crystallographically distinct ponatinib molecules, whereas 1D ^{1}H and 2D ^{1}H–^{1}H DQ–SQ spectra identify and assign the unusually deshielded imidazopyridazine proton. 1D ^{35}Cl spectra obtained at multiple fields confirm the presence of three distinct chloride ions, with density functional theory calculations providing key relationships between the SSNMR spectra and H···Cl^- hydrogen bonding arrangements. A 2D $^{35}Cl \rightarrow {}^{1}H$ D-RINEPT spectrum confirms the spatial proximities between the chloride ions, water molecules, and amine moieties. This all suggests future application of multinuclear SSNMR at high and ultra-high fields to the study of complex API solid forms for which SCXRD data are unavailable, with potential application to heterogeneous mixtures or amorphous solid dispersions.

Received 24th October 2023,
Accepted 26th January 2024

DOI: 10.1039/d3ce01062g

rsc.li/crystengcomm

Open Access Article. Published on 30 January 2024. Downloaded on 2/7/2026 1:11:04 PM.
This article is licensed under a Creative Commons Attribution-NonCommercial 3.0 Unported Licence.

1. Introduction

A significant body of research has been devoted to relating the crystal structures of active pharmaceutical ingredients (APIs) to their physicochemical properties.[1–4] Various classes of solid forms of APIs exist, including polymorphs, salts, hydrates/solvates, cocrystals, amorphous phases (including amorphous solid dispersions), and various combinations of these forms. Each solid form of an API can have divergent physicochemical properties, and can sometimes be marketed as distinct pharmaceutical products.[5,6] Because of the integral relationship between molecular-level structure and the properties of each solid form, there is significant interest in developing methods for the structural characterization of APIs. Full structural characterization provides useful information for rational design of novel solid forms, which can lead to improvements in drug efficacy, safety, and protection of intellectual property.[7,8]

Two common ways of modifying the physicochemical properties of an API are through the synthesis of salts (*i.e.*, solids exhibiting complete charge transfer between two or more molecular components) and cocrystals (*i.e.*, solids that are composed of two or more molecular and/or ionic components in the same crystal lattice, which are neither solvates or simple salts). Consequently, there is significant interest in studying the salt/cocrystal continuum,[9–11] especially as it relates to multicomponent crystals that are difficult to classify.[12] One uncommon group of API solid forms is those that contain an API with mixed charges on the

[a] *Apotex Pharmachem Inc., Brantford, ON, N3T 6B8, Canada*
[b] *Department of Chemistry & Biochemistry, Florida State University, Tallahassee, FL 32306, USA. E-mail: rschurko@fsu.edu*
[c] *National High Magnetic Field Laboratory, Tallahassee, FL 32310, USA*
[d] *MAX Diffraction Facility, McMaster University, Hamilton, ON, L8S 4M1, Canada*

† Electronic supplementary information (ESI) available. CCDC 2302285. For ESI and crystallographic data in CIF or other electronic format see DOI: https://doi.org/10.1039/d3ce01062g

‡ These authors have contributed equally.

Open Access Article. Published on 30 January 2024. Downloaded on 2/7/2026 1:11:04 PM.
This article is licensed under a Creative Commons Attribution-NonCommercial 3.0 Unported Licence.

counterion/coformer molecules. An example of this is the oxalate/oxalic acid salt cocrystal of escitalopram.[13] The crystal structure contains two escitalopram cations balanced by an oxalate dianion. Also included in the structure, hydrogen bonded to each side of the oxalate, are neutral molecules of oxalic acid, which produce linear supramolecular chains. Other examples include the hydrogen oxalate salt of ritonavir that cocrystallizes with oxalic acid,[14] and the tiotropium fumarate salt that cocrystallizes with fumaric acid,[15] both of which feature linear hydrogen oxalate/oxalic acid and/or fumarate/fumaric acid supramolecular chains. To the authors' knowledge, there are no examples of solid forms featuring mixed charges on API molecules. Although some progress has been made in the study of these materials, a more complete understanding of the structures of materials falling within the salt/cocrystal continuum would benefit from the advancement of spectroscopic methods for the structural characterization of API solid forms.[8,16–21]

Solid-state NMR (SSNMR) spectroscopy is a powerful technique for the structural characterization of APIs, as it can greatly augment the understanding of molecular-level structure obtained by other methods such as X-ray diffraction (XRD).[22] In this regard, NMR crystallography has the potential to provide insight into crystal structures in the absence of high-quality diffraction data,[23–34] making the analysis of NMR spectra in terms of structural features a topic of considerable recent investigation.[35–40] 1D and/or 2D ^{13}C SSNMR experiments are among the most commonly used, that when paired with quantum chemical calculations using density functional theory (DFT), provide site-specific chemical information that can be linked directly to molecular-level structure.[38,41] However, these methods have limited applications for large molecules with many carbon atoms, where definitive spectral assignments often cannot be made. Furthermore, measurement of the isotropic chemical shifts alone may not provide rich structural information related to intermolecular bonding arrangements (although this could be obtained through measurement of the principal values of chemical shift tensors or through other 2D techniques).[22] ^{13}C SSNMR also has limited applicability for the study of API dosage forms where interfering signals arise from excipient molecules (especially for those of low API wt%). ^{1}H SSNMR techniques also suffer from similar disadvantages, which are compounded by the smaller chemical shift range and the common presence of strong homonuclear dipolar coupling, which broadens spectral lines, even under conditions of moderate or fast magic angle spinning (MAS).[42]

When an API is formulated as a hydrochloride (HCl) salt (which accounts for nearly half of oral dosage forms),[43] ^{35}Cl (nuclear spin, I = 3/2) SSNMR spectroscopy is invaluable for characterizing the local hydrogen bonding environments of chloride ions.[44–55] This sensitivity results from the fact that electric field gradients (EFGs) at the chlorine nucleus are extremely sensitive to ground-state electron density, as reflected in the appearance of the corresponding ^{35}Cl SSNMR central transition (CT, +1/2 ↔ −1/2) powder patterns, which are typically influenced by the second-order quadrupolar interaction. Furthermore, the number of magnetically distinct chloride ions in an API solid form is typically small, meaning that spectra can be readily assigned and interpreted in terms of their local H···Cl$^-$ hydrogen bonding environments.[44–50] ^{35}Cl SSNMR methods also have the ability to identify chemical changes that occur within dosage forms (*e.g.*, the uptake of atmospheric water or the disproportionation of ions due to interactions with excipients),[56,57] quantify the wt% API in dosage forms,[46,56] and even characterize static and/or dynamic disorder in solids.[58] Various 2D SSNMR techniques that exploit (ultra)fast MAS and indirect detection of low-γ nuclides have been developed in recent years,[59–63] which could enhance understanding of H···Cl$^-$ hydrogen bonding arrangements and their complex relationships with ^{35}Cl EFG tensors. Finally, the advent of ultra-high field NMR (*e.g.*, using fields up to 35.2 T), possibly augmented through use of MQMAS techniques,[64–66] is expected to advance applications of ^{35}Cl SSNMR spectroscopy for the study of complex API solid forms with multiple overlapping patterns, including heterogeneous mixtures and amorphous solid dispersions.

This study focuses on a novel solid form of the API ponatinib hydrochloride, 3-[2-(imidazo[1,2-*b*]pyridazin-3-yl)ethynyl]-4-methyl-*N*-{4-[(4-methylpiperazin-1-yl)methyl]-3-(trifluoromethyl)-phenyl}benzamide hydrochloride (Scheme 1), a tyrosine-kinase inhibitor used for the treatment of leukemia.[67,68] At least eight different solid forms of ponatinib have been reported,[69–71] including one form that is used in the branded drug product Iclusig.[72–74] We report the synthesis and characterization of a ionic cocrystal of ponatinib HCl, (hereafter referred to as **pon·HCl**),[75] which features an unusual stoichiometry with an asymmetric unit containing both a monocation and a dication of the ponatinib molecule, three water molecules, and three chloride ions. The crystal structure is obtained through single-crystal X-ray diffraction, and the uncommon structural features are verified through multinuclear and multidimensional SSNMR spectroscopy, with an emphasis on ^{35}Cl NMR spectra acquired at fields up to 35.2 T. DFT calculations are used to refine the crystal structure, assign peaks in the complex ^{1}H and ^{13}C SSNMR spectra, and provide relationships between the molecular-level structure and ^{35}Cl SSNMR spectra. We emphasize that

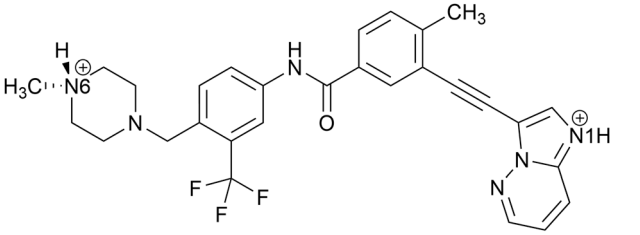

Scheme 1 Molecular structure of ponatinib, showing the two possible sites of protonation. The ponatinib monocation is protonated at the position of N6, whereas the dication is protonated at N6 and N1.

 This journal is © The Royal Society of Chemistry 2024

Open Access Article. Published on 30 January 2024. Downloaded on 2/7/2026 1:11:04 PM.
This article is licensed under a Creative Commons Attribution-NonCommercial 3.0 Unported Licence.

this is the only solid form of ponatinib to be characterized by either XRD or SSNMR methods to date. Finally, we discuss the significance of the discovery of this unusual ionic cocrystal, its wider implications to the crystal engineering and pharmaceutical communities, and the utility of high-field SSNMR spectroscopy for the characterization of such materials.

2. Experimental

2.1. Synthesis

Synthesis of pon·HCl on from ponatinib monohydrochloride. Ponatinib monohydrochloride (501 mg, 0.88 mmol) was weighed into a round bottom flask, to which was added acetonitrile (5.0 mL) and formic acid (0.35 mL). The resulting suspension was placed in an oil bath at 50 °C. After stirring for 1 h, water (0.50 mL) was added. Immediate dissolution was observed, the resulting yellow solution was filtered while hot, and subsequently allowed to cool to room temperature (RT) over a 1.5 h period. Precipitation was observed after 2 h at RT. The suspension was stirred for an additional 16 h. The solids were collected by filtration, washed with cold acetonitrile (2.0 mL), and dried in a vacuum oven at RT to give **pon·HCl** as a yellow solid (248 mg, 50% yield).

Synthesis of pon·HCl from the freebase. Ponatinib freebase (83.8 g) was suspended in acetone (314 mL) and water (70 mL) at RT. HCl (aq) (19.17 g, 1.0 mol eq.) was added to the mixture. After stirring at RT for 30 min, the suspension was heated to 45–50 °C for 30 min, leading to complete dissolution. Formic acid (29.3 mL) was added, and the solution was stirred for 30 min. The solution was cooled to 20 °C, held at that temperature for 1 h, further cooled to 0–5 °C, and stirred for 16 h. The resulting precipitate was filtered and washed with cold acetone (168 mL). The yellow solid was dried in a vacuum oven at 55 °C for 3 h, to give **pon·HCl** (69.63 g, 83% yield).

Single crystal growth. Crystals of **pon·HCl** suitable for analysis by single-crystal X-ray diffraction (SCXRD) were grown in an unconventional manner. Ponatinib freebase was added to a 4 mL vial, and acetonitrile was added on top of the solid material until covered. 1 mL of a solution prepared from acetonitrile (10 mL), formic acid (0.7 mL), water (0.8 mL), and hydrochloric acid (concentrated, 0.2 mL) was then layered over the first acetonitrile solution in the vial. After two days at RT, both white needle and yellow block crystals were seen in the vial. The crystals were carefully separated using the Pasteur method, and PXRD data were acquired for each type of crystal. The yellow block crystals were found to be **pon·HCl**, and the white needles were found to be the previously reported ponatinib monohydrochloride.[69,70]

2.2. Single crystal X-ray diffraction

SCXRD studies were conducted at the MAX facility at McMaster University (Hamilton, ON, Canada). A suitable crystal fragment was selected and frozen on a MiTeGen loop using *n*-paratone oil on a Bruker APEX-II CCD diffractometer with a Mo Kα radiation source. The temperature was kept at 100 K during data collection. Using OLEX2,[76] the structure was solved with the XT[77] structure solution program using intrinsic phasing and refined with the XL[78] refinement package using least squares minimization. The structure has been deposited in the Cambridge Structural Database under the deposition number 2302285 with database identifier PONLOX.

2.3. Solid-state NMR spectroscopy

Overview. Preliminary low-field SSNMR experiments were conducted at the University of Windsor (Windsor, ON, Canada) using a 9.4 T wide-bore Oxford magnet and a Bruker Avance III HD spectrometer with Larmor frequencies of $\nu_0(^1H)$ = 400.24 MHz and $\nu_0(^{35}Cl)$ = 39.22 MHz, and a revolution 5.0 mm HX static probe with the sample packed into 5.0 mm o.d. glass tubes. All high-field SSNMR spectra were acquired at the National High Magnetic Field Laboratory (NHMFL, Tallahassee, FL). Spectra obtained at 18.8 T used medium-bore Oxford magnets and a Bruker Avance III HD console for which $\nu_0(^1H)$ = 800.12 MHz, $\nu_0(^{13}C)$ = 201.19 MHz, and $\nu_0(^{35}Cl)$ = 78.39 MHz, or a Bruker Avance NEO console with $\nu_0(^1H)$ = 799.74 MHz and $\nu_0(^{35}Cl)$ = 78.36 MHz. Static and MAS experiments were conducted using a Low-E 3.2 mm HXY MAS probe (designed and constructed at the NHMFL) with the sample packed into a 3.2 mm o.d. pencil-style zirconia rotor. Ultrafast MAS experiments used a Bruker 1.3 mm HCN MAS probe (with the ^{15}N channel tuned to ^{35}Cl), or a NHMFL-built 1.3 mm HXY MAS probe with the sample packed into a 1.3 mm o.d. Bruker-style rotor. Spectra obtained at 35.2 T used the series-connected hybrid (SCH) magnet[79] and a Bruker Avance NEO console for which $\nu_0(^1H)$ = 1500.21 MHz and $\nu_0(^{35}Cl)$ = 146.98 MHz. Experiments used a NHMFL-built Low-E 3.2 mm HX MAS probe with the sample packed into a 3.2 mm o.d. pencil-style rotor. A summary of all acquisition parameters is provided in the ESI† (Tables S1–S4).

All spectra were processed and fit using the ssNake v1.3 software package.[80] Uncertainties in the EFG and chemical shift tensor parameters and Euler angles were assessed *via* bidirectional variation of each parameter, and visual comparison of experimental and simulated spectra.

^{13}C NMR spectra. A $^1H \rightarrow {}^{13}C\{^1H\}$ ramped-amplitude cross polarization (CP)/MAS sequence[81–84] was used to obtain the ^{13}C SSNMR spectra, featuring a ^1H π/2 pulse of 3.33 μs, SPINAL-64 ^1H decoupling with ν_2 = 75 kHz,[85] a spinning rate of ν_{rot} = 18 kHz, a contact time of 2.0 ms with a Hartmann–Hahn matching field (50 kHz on the H channel, and matched on the X channel),[86] and a recycle delay of 30 s. Chemical shifts were referenced to neat TMS at $\delta_{iso}(^{13}C)$ = 0.0 ppm using the high-frequency peak of α-glycine at $\delta_{iso}(^{13}C)$ = 176.5 ppm as a secondary reference.[87]

^1H NMR spectra. ^1H spectra were acquired at 18.8 T using ν_{rot} = 50 kHz, π/2 pulse widths of 2.5 μs, and a relaxation delay of 6.5 s. The 1D spectrum was collected using a Hahn-echo sequence with 8 coadded transients. The ^1H DQ–SQ

Open Access Article. Published on 30 January 2024. Downloaded on 2/7/2026 1:11:04 PM. This article is licensed under a Creative Commons Attribution-NonCommercial 3.0 Unported Licence.

spectrum was acquired using one rotor period of back-to-back (BABA) recoupling,[88,89] 48 t_1 increments, and 16 coadded transients per increment. Chemical shifts were referenced to neat TMS at $\delta_{iso}(^1H) = 0.0$ ppm, using the high-frequency peak in L-histidine HCl·H_2O at $\delta_{iso}(^1H) = 17.2$ ppm.[61]

^{35}Cl NMR spectra. The ^{35}Cl spectra acquired at 9.4, 18.8, and 35.2 T used a Hahn-echo sequence with CT-selective $\pi/2$ pulses, with ^{1}H decoupling used for experiments at 9.4 and 18.8 T. The MAS experiment at 35.2 T used a spinning rate of ν_{rot} = 16 kHz. Chemical shifts were referenced to 0.1 M NaCl in D_2O at $\delta_{iso}(^{35}Cl) = 0.0$ ppm using NaCl(s) at $\delta_{iso}(^{13}C) = 41.1$ ppm as a secondary reference.

^{35}Cl → ^{1}H D-RINEPT Spectrum. A 2D ^{35}Cl → ^{1}H spectrum was obtained at 18.8 T using the dipolar-mediated refocused insensitive nuclei enhanced by polarization transfer (D-RINEPT) sequence.[60,90] The spectrum was obtained with ν_{rot} = 50 kHz, a recycle delay of 0.5 s, 64 t_1 increments, and 4096 scans per increment. A 5.0 μs CT-selective $\pi/2$ pulse was applied on the ^{35}Cl channel. Rotor-synchronized dipolar recoupling was applied on the ^{1}H channel using symmetry-based $SR4_1^2$ recoupling[91] with an rf field equivalent to two times ν_{rot} to fulfill the second-order R^3 condition, which was calibrated through a separate ^{1}H $\pi/2$ pulse-spin lock pulse experiment.[92] Enhanced CT-polarization was achieved through WURST pulse blocks applied on the ^{35}Cl channel prior to the D-RINEPT transfer step, using WURST-80 pulses with a 38.0 μs duration (followed by a 2.0 μs delay), a maximum rf of 30 kHz, a 50 kHz sweep width, and an optimized transmitter offset frequency of 300 kHz.[93,94]

2.4. Additional characterization techniques

Additional characterization techniques, including powder XRD (PXRD), thermal gravimetric analysis (TGA), differential scanning calorimetry (DSC), potentiometric titrations, and solution-state ^{1}H NMR spectroscopy, are described in the ESI† S1.

2.5. Density functional theory calculations

Geometry optimizations. Plane-wave DFT calculations were performed using the CASTEP module within BIOVIA Materials Studio 2020 (ref. 95) using the single-crystal X-ray diffraction data for **pon·HCl** as an initial structural model. These calculations used the RPBE functional,[96] ultrasoft pseudopotentials generated on-the-fly,[97] a plane-wave cutoff energy of 800 eV, and a Monkhorst–Pack grid with a *k*-point spacing of 0.05 Å^{-1}.[98] Structural refinements employed the LBFGS energy-minimizing scheme,[99] with convergence thresholds including a maximum change in energy of 5×10^{-6} eV per atom, a maximum displacement of 5×10^{-4} Å per atom, and a maximum Cartesian force of 10^{-2} eV Å^{-1}. Dispersion corrections were introduced using the semi-empirical two-body dispersion force field correction of Grimme (DFT-D2),[100,101] or a reparametrized version of this method introduced by the authors for applications in NMR crystallography (DFT-D2*).[102–104] These calculations used a two-step geometry optimization in which all atoms were first relaxed at the RPBE-D2 level (s_6 = 1.0; d = 20.0), followed by a second optimization in which only atoms involved in X–H···Cl$^-$ (X = N, O) hydrogen bonding were relaxed at the RPBE-D2* level (s_6 = 1.0; d = 3.5), while all other atoms remained in fixed positions. This refined crystal structure was used in all subsequent computational analyses.

Thermochemistry. Single-point energy calculations were performed using the Amsterdam Modeling Suite (AMS 2021.106), in which a dimer of ponatinib molecules was used as a structural model to calculate the potential energy as a function of the intermolecular NH$^+$···N hydrogen bond distance. These calculations employed the double-hybrid PBE0-2 functional,[105] which combines a 79% admixture of Hartree–Fock exchange and a 50% admixture of Møller–Plesset correlation with the PBE functional. Semiempirical dispersion was introduced through the three-body B3(BJ) model (s_6 = 0.540; s_8 = 0.515; a_1 = 0; a_2 = 8.345).[106,107] These calculations employed the TZ2P basis set with Becke integration set to "very good".[108,109]

Magnetic shielding and EFG tensors. Magnetic shielding tensors were calculated in CASTEP using the gauge-including projector-augmented wave (GIPAW) method[110] and AMS using the gauge-including atomic orbital (GIAO) method.[111–115] CASTEP calculations used structural models consisting of the fully periodic crystal structure or an isolated molecule, whereas AMS calculations were performed on isolated molecules only. CASTEP calculations of EFG and magnetic shielding tensors used the RPBE functional,[96] ultrasoft pseudopotentials generated on-the-fly,[97] a plane-wave cutoff energy of 800 eV, and a Monkhorst–Pack grid with a *k*-point spacing of 0.05 Å^{-1}.[98] AMS calculations of magnetic shielding tensors used the TZ2P basis set, with Becke integration set to "very good",[108,109] along with the hybrid PBE0 functional,[116] which includes a 25% admixture of Hartree–Fock exchange.

^{35}Cl EFG and magnetic shielding tensors were calculated through a single periodic calculation using CASTEP. In contrast, ^{1}H and ^{13}C magnetic shielding tensors were obtained from three separate calculations: (i) a RPBE calculation in CASTEP using the periodic crystal lattice as a structural model; (ii) a RPBE calculation in CASTEP using only an isolated molecule, which was approximated using a *P*1 unit cell with a size of 25 × 25 × 25 Å; and (iii) a final PBE0 calculation in AMS using an isolated molecule as the structural model. The difference between the first two calculations provides the intermolecular contributions to the ^{1}H and ^{13}C chemical shifts, which are added to the higher level PBE0 calculation performed in AMS. The advantage of this method rests on the fact that magnetic shielding is largely a local phenomenon, meaning that the influences of weak noncovalent interactions on magnetic shielding tensors can be calculated at a tractable lower level.

^{1}H, ^{13}C, and ^{35}Cl magnetic shielding constants were converted to their respective chemical shift scales through additional calculations on small organic molecules and

 This journal is © The Royal Society of Chemistry 2024

Open Access Article. Published on 30 January 2024. Downloaded on 2/7/2026 1:11:04 PM.
This article is licensed under a Creative Commons Attribution-NonCommercial 3.0 Unported Licence.

comparison with previously published experimental chemical shifts (ESI† S2).[62,117–120] Euler angles describing the relative orientation of the chemical shift and EFG tensors, according to the *ZY′Z″* convention for rotation, were extracted from the CASTEP output files using EFGShield 4.1.[121]

3. Results and discussion

3.1. Synthesis and preliminary characterization

A novel solid form of the API ponatinib hydrochloride (**pon·HCl**) was synthesized from both ponatinib monohydrochloride and freebase ponatinib as reagents, with the former yielding powder samples, and the latter yielding either powders or large crystals, depending on the experimental conditions. All three synthetic pathways led to formation of the same novel product, as indicated by PXRD (Fig. 1). It was initially assumed that **pon·HCl** was simply a novel polymorph or hydrate of ponatinib monohydrochloride; however, subsequent analyses demonstrated that this was not the case.

The structure of **pon·HCl** was determined by SCXRD, and found to be a complex multicomponent crystal featuring a ponatinib monocation, a ponatinib dication, three chloride ions, and three water molecules (*vide infra*). However, prior to the determination of the crystal structure and the precise establishment of the stoichiometry of various molecular and ionic components, several analytical techniques indicated that **pon·HCl** is a hydrate, and does not feature the anticipated 1.0 eq. of Cl^- to 1.0 eq. of ponatinib for a monohydrochloride salt. Powder samples of **pon·HCl** appear to be stable under ambient conditions and are unaffected by humidity. The DSC thermogram shows a broad, major endotherm with an onset at 175.4 °C, further indicating the stability of **pon·HCl** near RT (Fig. S1†). Analysis by TGA indicates a gradual reduction in mass of 4.4% during heating from *ca.* 30–175 °C, which is consistent with a loss of 1.5 eq. of H_2O relative to the 1.0 eq. of ponatinib (Fig. S2†). A potentiometric titration for Cl^- ions showed 8.50% Cl^- in the material, which is close to the 8.66% that would indicate 1.5 eq. of Cl^- with respect to the 1.0 eq. of ponatinib. The ^{1}H NMR (acetic acid-d_3) spectrum showed that *ca.* 0.06 wt% formic acid was retained in the final solid products (Fig. S3†) (N.B.: the role of formic acid in crystal nucleation is unknown, except for the fact that without it, **pon·HCl** is not formed. It may be that interactions involving formic acid, ponatinib, and other constituents play key roles in pre-organization, nucleation, and/or crystallization).

The consistent observation of 1.5 eq. of Cl^- (indicated by potentiometric titrations) and 1.5 eq. of H_2O (indicated by TGA) relative to the 1.0 eq. of ponatinib that would be anticipated for a monohydrochloride salt led us to reconsider the optimal synthetic conditions for preparing **pon·HCl**. To rule out the possibility that the excess Cl^- arises from interstitial sources (*e.g.*, aqueous HCl), additional efforts were made to remove the excess chloride. Syntheses using <1.5 eq. of Cl^- resulted in lower yields, but still with 1.5 eq. of Cl^-. Attempts to dry the material further using higher temperatures and stronger vacuum resulted in a reduction to 1.3 eq. of Cl^- in the final solid product, but with significant decreases in crystallinity (as indicated by PXRD). In the end, it was clear that the excess 0.5 eq. of chloride could not be removed without compromising the crystallinity of the solid form, and that a novel solid form had been produced with a stoichiometry distinct from that of a monohydrochloride salt. Therefore, an effort was made to characterize **pon·HCl** through the combination of SCXRD and multinuclear SSNMR spectroscopy.

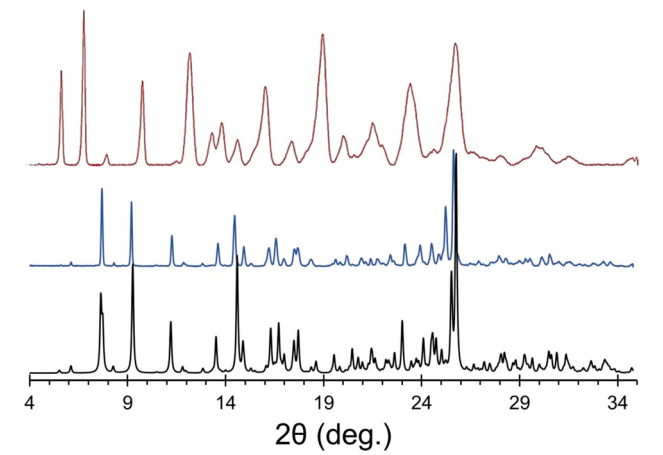

Fig. 1 Experimental PXRD patterns of ponatinib monohydrochloride form I (red), the novel form **pon·HCl** (blue), and a simulated pattern based on the crystal structure of **pon·HCl**. There are some systematic differences in the peak positions in the experimental powder pattern of **pon·HCl** and the simulated pattern based on its crystal structure (especially at high 2θ angles), because the two datasets were obtained at 298 K and 100 K, respectively.

3.2. Crystal structure and refinement

Pon·HCl crystallizes in the triclinic space group $P\bar{1}$ (Table 1) with a structure that is composed of one ponatinib monocation, one ponatinib dication, three chloride anions, and three water molecules in the asymmetric unit (Fig. 2; see Fig. S4† for an overlay of the two ponatinib molecules), which is consistent with the preliminary observations made through TGA and potentiometric titrations. Both the mono- and dications of the ponatinib molecule are protonated on the methyl piperazine nitrogens (N6B and N6A, respectively), each forming a hydrogen bond with the nearby chloride ions (Cl1B and Cl1A, respectively). The dication molecule features an additional protonated nitrogen atom (N1A) within the imidazopyridazine moiety, with the associated hydrogen atom (H1A) found to be hydrogen bonded to the equivalent nitrogen atom (N1B) in the monocation (Fig. 3A). H1A was located in the difference map with a strong diffraction peak and refined as an isotropic hydrogen atom, causing a subsequent R_1 drop, casting no doubt as to which nitrogen atom is protonated (N1A).

Unusually, the third chloride ion (Cl1) was not located in the vicinity of hydrogen atoms associated with the positively charged protonated imidazopyridazine, charged amine, or

Open Access Article. Published on 30 January 2024. Downloaded on 2/7/2026 1:11:04 PM.
This article is licensed under a Creative Commons Attribution-NonCommercial 3.0 Unported Licence.

Table 1 Single-crystal X-ray diffraction data and refinement parameters for **pon·HCl**

CCDC no.	2302285	V (Å^3)	2907.9(3)
Formula	$C_{58}H_{63}Cl_3F_6N_{12}O_5$	Z	2
Formula weight (g mol^{-1})	1228.55	ρ_{calc} (g cm^{-3})	1.403
Crystal system	Triclinic	μ (mm^{-1})	0.237
Space group	$P\bar{1}$ (no. 2)	Reflections collected	97 752
T (K)	100.0(1)	Independent reflections	14 060 (R_{int} = 0.0692, R_σ = 0.0588)
a (Å)	12.4408(7)	Restraints/parameters	0/790
b (Å)	15.1905(8)	$R_1[I > 2\sigma(I)]$	0.0599
c (Å)	16.5411(9)	R_1 (all data)	0.0894
α (°)	92.864(3)	wR_1 (all data)	0.1724
β (°)	102.624(3)	GoF on F^2	1.096
γ (°)	106.246(3)	Largest diff. peak/hole (e Å^{-3})	0.67/−0.40

amide moieties. In fact, Cl1 does not form hydrogen bonds with any organic moiety within the ponatinib molecules, with only a weak noncovalent interaction involving the aromatic proton H1AA at r(CH···Cl$^-$) = 2.573 Å. However, Cl1 forms hydrogen bonds with two of the H_2O molecules, which each hydrogen bond with a third H_2O molecule, forming a "square" arrangement (Fig. 3B). The hydrogen atoms of the H_2O molecules were added in calculated positions, with the rigid H_2O groups oriented as indicated by the difference map peaks. The final electron density difference map gave no indication that any of the three H_2O molecules are protonated to form H_3O^+ ions.

The crystal structure of **pon·HCl** was subjected to a dispersion-corrected plane-wave DFT geometry optimization in which all atomic positions were refined in a two-step process (*vide supra*), with the unit cell parameters fixed at their experimental values. All interatomic distances and calculated NMR interaction tensors reported in this work are determined from this refined crystal structure. Additionally, double-hybrid PBE0-2/D3(BJ) DFT calculations were used to confirm the position of H1A by varying its position along the bonding axis of the intermolecular NH$^+$···N hydrogen bond (Fig. 4). These calculations indicate a double-well potential energy surface, with an activation barrier of 18.5 kJ mol^{-1} with respect to the global energy minimum.

3.3. SSNMR spectroscopy

^{1}H → ^{13}C{^{1}H} SSNMR spectra. The ^{1}H → ^{13}C{^{1}H} spectrum acquired at 18.8 T and a ν_{rot} = 18 kHz features many overlapping peaks (Fig. 5A), consistent with the 54 crystallographically distinct carbon atoms observed in the crystal structure. A preliminary assignment of the peaks is

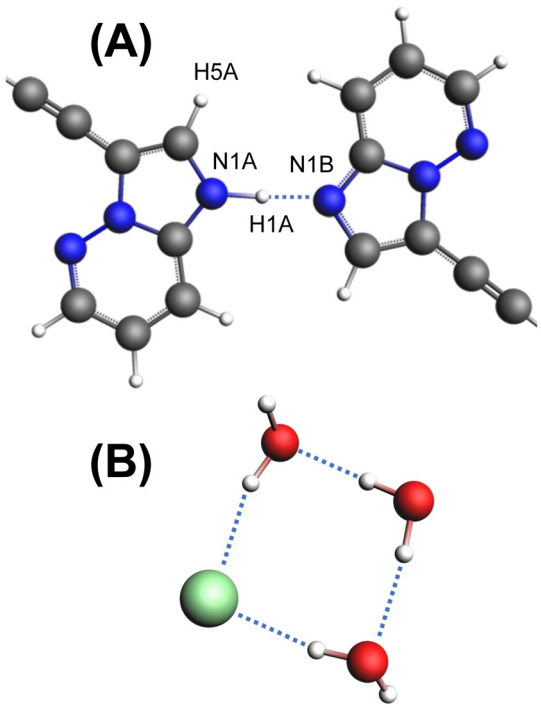

Fig. 3 (A) The hydrogen bonding motif of the two imidazopyridazine rings, with atom labels indicated. (B) The hydrogen bonding motif of Cl1 and three H_2O molecules.

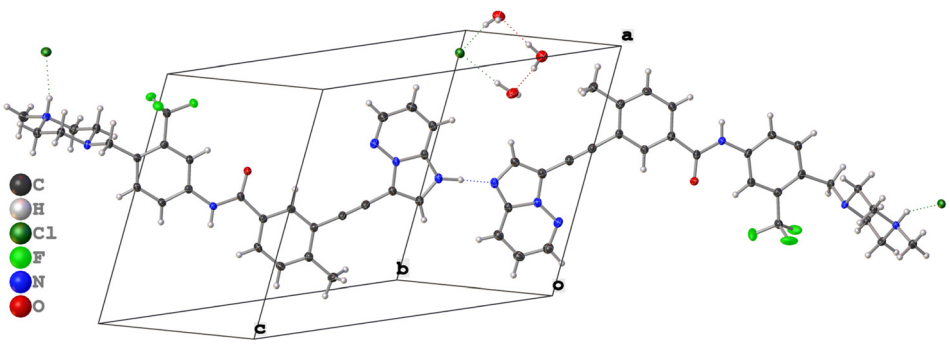

Fig. 2 The structure of **pon·HCl**, as determined by single-crystal X-ray diffraction.

 This journal is © The Royal Society of Chemistry 2024

Open Access Article. Published on 30 January 2024. Downloaded on 2/7/2026 1:11:04 PM.
This article is licensed under a Creative Commons Attribution-NonCommercial 3.0 Unported Licence.

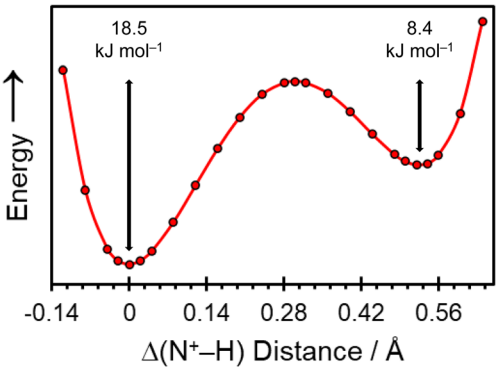

Fig. 4 Potential energy curve describing the position of the hydrogen atom within the intermolecular $NH^+\cdots N$ hydrogen bond in **pon·HCl**, as predicted using DFT calculations at the double-hybrid PBE0-2/D3(BJ) level. The value of $\Delta(N^+–H)$ designates the distance of the hydrogen atom with respect to the global energy minimum at $\Delta(N^+–H)$ = 0 Å.

made through DFT calculations (Fig. 5B), with a complete listing of all DFT calculated ^{13}C chemical shifts provided in Table S5.† In general, it is only possible to assign the carbon sites to specific structural moieties, rather than to signals arising from crystallographically and magnetically distinct sites. Nonetheless, the observation of pairs of peaks (*i.e.*, peak doubling in some cases) is evidence for the two crystallographically distinct ponatinib molecules in the crystal structure of **pon·HCl**. Additional experiments involving dipolar dephasing, or other spectral editing techniques, or possibly 2D techniques, could potentially lead to the assignments of a larger number of ^{13}C peaks to chemically similar but magnetically distinct sites.

^{1}H and ^{1}H–^{1}H DQ–SQ SSNMR spectra. The 1D ^1H SSNMR spectrum acquired at 18.8 T and ν_{rot} = 50 kHz features regions of strongly overlapping peaks, corresponding to the 63 crystallographically distinct hydrogen atoms in the asymmetric unit, most of which cannot be resolved or assigned definitively (Fig. 5C). A complete listing of all DFT calculated ^1H chemical shifts is provided in Table S6.† The resolved peak at $\delta_{iso}(^1H)$ = 18.8 ppm is assigned to the key

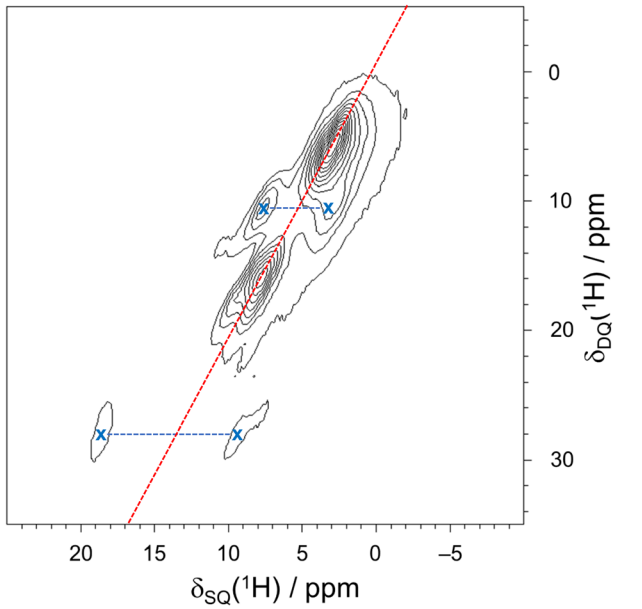

Fig. 6 A 2D ^1H–^1H DQ–SQ spectrum of **pon·HCl** acquired at 18.8 T with ν_{rot} = 50 kHz and one rotor period of BABA recoupling. The red diagonal line representing the relationship $\delta_{DQ} = 2\delta_{SQ}$ is included as a visual aid. Connected off-diagonal peaks are indicated by blue horizontal lines and X's.

imidazopyridazine proton (H1A), which is covalently bound to N1A in the ponatinib dication, and forms an intermolecular hydrogen bond with N1B in the monocation, leading to the high chemical shift that is indicative of a very deshielded proton (in agreement with DFT calculations, Fig. 5D).

A ^1H–^1H DQ–SQ spectrum, acquired at 18.8 T with ν_{rot} = 50 kHz and one rotor period of BABA recoupling, provides some additional resolution of ^1H spectral peaks (Fig. 6). In such an experiment, the ^1H–^1H homonuclear dipolar coupling is recoupled during the double quantum excitation and reconversion periods, leading to the observation of correlations between spatially proximate ^1H spins. Because the recoupling time is short, only the strongly coupled sites appear in the 2D spectrum. Peaks appear along the δ_{DQ} =

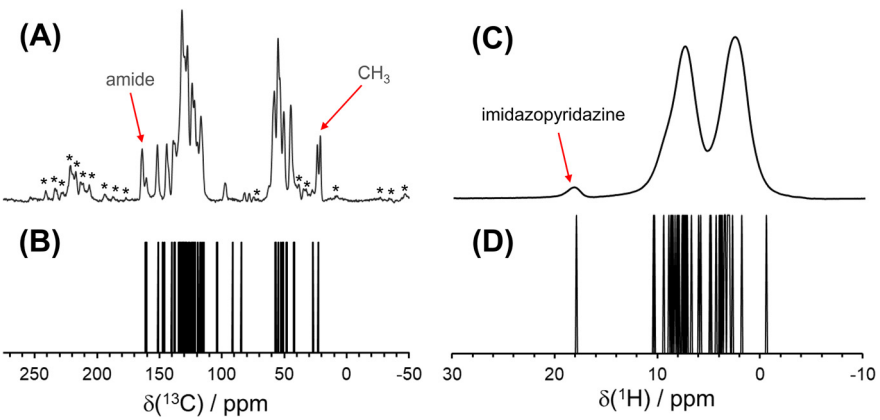

Fig. 5 (A) High-resolution $^1H \rightarrow {}^{13}C\{^1H\}$ CP/MAS spectrum of **pon·HCl** acquired at 18.8 T with ν_{rot} = 18 kHz. Spinning sidebands are marked by asterisks (*). (B) Simulated ^{13}C spectrum based on DFT calculations. (C) 1D ^1H Hahn echo spectrum of **pon·HCl** acquired at 18.8 T with ν_{rot} = 50 kHz. (D) Simulated ^1H spectrum based on DFT calculations.

Open Access Article. Published on 30 January 2024. Downloaded on 2/7/2026 1:11:04 PM.
This article is licensed under a Creative Commons Attribution-NonCommercial 3.0 Unported Licence.

$2\delta_{SQ}$ diagonal line when (i) two crystallographically equivalent protons are close enough to produce through-space dipolar correlations or (ii) short-range correlations are observed between two nearby protons with the same chemical shift.[122] Correlations between protons with different chemical shifts manifest as pairs of peaks that are equidistant from the diagonal line with a value of δ_{DQ} equal to the sum of the two distinct values of δ_{SQ}. The spectrum has clear off-diagonal peaks (marked with X) that demonstrate correlations between the well-resolved imidazopyridazine proton (H1A) and its nearest neighbor, H5A ($\delta_{iso}(^1H)$ = 10.6 ppm), which is predicted by DFT calculations to have the highest shift of the remaining protons. Additional off-diagonal peaks suggest correlations involving protons in the charged amine moieties, water molecules, and various species of aliphatic protons; however, clear features are not present that lend further insight into these relationships.

^{35}Cl and ^{35}Cl → ^{1}H D-RINEPT SSNMR spectra. ^{35}Cl SSNMR spectra were acquired under static conditions at 9.4 and 18.8 T, and under both static and MAS conditions at 35.2 T (Fig. 7). Of these, only the spectra acquired at 18.8 and 35.2 T were useful for determining the EFG and chemical shift tensors (*vide infra*). Spectra were acquired at multiple fields because the chemical shift interaction and second-order quadrupolar interaction (SOQI) have field-dependent manifestations in the CT patterns of half-integer quadrupolar nuclides (HIQNs) that scale in proportion to B_0 and B_0^{-1}, respectively. Typically, acquisition of spectra with sufficiently high MAS rates averages the chemical shift interaction and partially averages the SOQI, leading to CT powder patterns that are influenced by only three parameters: the isotropic chemical shift, δ_{iso}; quadrupolar coupling constant, C_Q; and asymmetry parameter, η_Q. Acquisitions of static spectra at two fields allows for the determination of additional parameters describing the chemical shift tensor (span, Ω; skew, κ) and the set of Euler angles (α, β, γ) defining the relative orientation of the principal axis systems of the EFG and chemical shift tensors (see Table 2 for definitions).

The 1D ^{35}Cl SSNMR spectra indicate the presence of three overlapping patterns, corresponding to the three crystallographically and magnetically distinct chloride ions in the crystal lattice of **pon·HCl** (see Fig. 8 for a deconvolution of the 35.2 T MAS spectrum and Table 2 for NMR tensor parameters). The three overlapping patterns in the ^{35}Cl SSNMR spectra are readily assigned to their respective crystallographic sites through use of plane-wave DFT calculations due to the substantial differences in the EFG and chemical shift tensors (*vide infra*). In the 35.2 T MAS spectrum, the three patterns have relative integrated intensities of 1.0 : 1.0 : 0.9, which is close to the anticipated ratio of 1 : 1 : 1 (Cl1 : Cl1A : Cl1B). The spectra show no evidence of impurity phases, including the products of disproportionation reactions; this conclusion is further supported by the absence of any sharp peaks in Bloch decay spectra acquired at 9.4 T, using relaxation delays of 1.0 and 8.0 s (Fig. S5†).

The comparison of ^{35}Cl static Hahn-echo spectra acquired at 9.4, 18.8, and 35.2 T demonstrates a striking example of the utility of ultra-high field SSNMR for the analysis and structural characterization of APIs with unusual crystal structures and correspondingly complex SSNMR spectra. Only the spectra acquired at 18.8 and 35.2 T have patterns of high enough quality from which EFG and chemical shift tensor

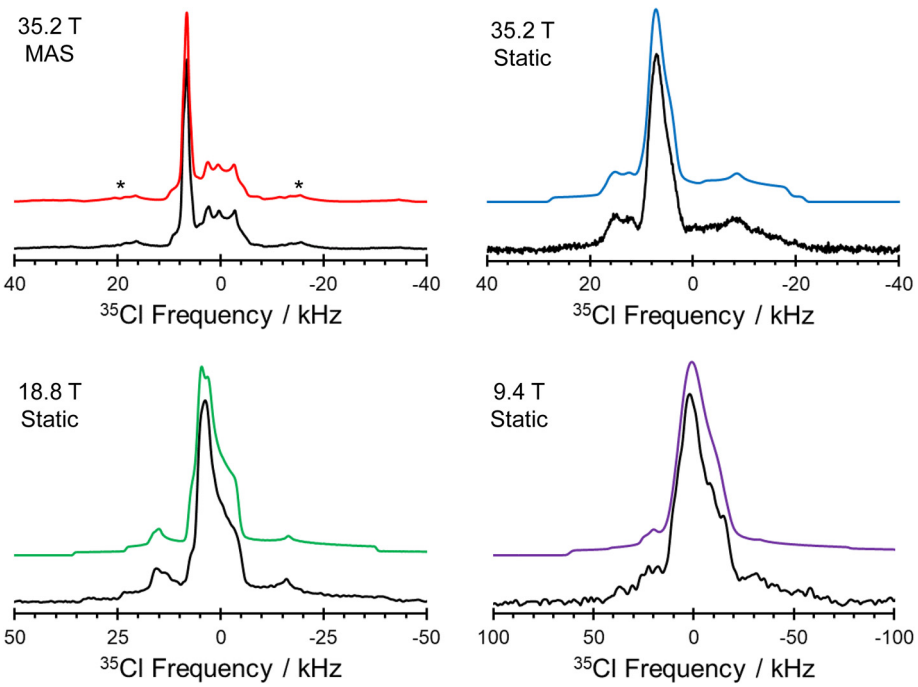

Fig. 7 Experimental ^{35}Cl SSNMR spectra of **pon·HCl**. Spectra of static samples were acquired at 9.4 T, 18.8 T, and 35.2 T, as well as under MAS (ν_{rot} = 16 kHz) conditions at 35.2 T. Spinning side bands are marked by asterisks (*).

 This journal is © The Royal Society of Chemistry 2024

Open Access Article. Published on 30 January 2024. Downloaded on 2/7/2026 1:11:04 PM. This article is licensed under a Creative Commons Attribution-NonCommercial 3.0 Unported Licence.

Table 2 Summary of calculated and experimental ^{35}Cl EFG and chemical shift tensor parameters for **pon·HCl**[a,b,c,d,e]

		C_Q (MHz)	η_Q	δ_{iso} (ppm)	Ω (ppm)	κ	α (°)	β (°)	γ (°)
Cl1	Exp.	2.21(4)	0.70(4)	52(2)	30(10)	—[f]	—[f]	100(20)	—[f]
	DFT-D2*	2.51	0.47	84	26	0.65	181	80	98
ClA	Exp.	5.13(6)	0.40(5)	25(2)	80(10)	0.2(2)	90(10)	0(15)	10(5)
	DFT-D2*	−4.79	0.70	42	90	0.0	70	7	0
ClB	Exp.	5.66(6)	0.71(5)	70(2)	70(10)	—[f]	—[f]	0(5)	—[f]
	DFT-D2*	−5.85	0.61	93	88	−0.10	98	40	1

[a] Theoretical EFG and chemical shift tensor parameters were obtained from calculations on XRD-derived structures and structures refined at the RPBE-D2* level. [b] The experimental uncertainties in the last digit for each value are indicated in parentheses. [c] The principal components of the EFG tensors are defined such that $|V_{33}| \geq |V_{22}| \geq |V_{11}|$. The quadrupolar coupling constant and asymmetry parameter are given by $C_Q = eQV_{33}/h$, and $\eta_Q = (V_{11} - V_{22})/V_{33}$, respectively. The sign of C_Q cannot be determined from the experimental ^{35}Cl spectra. [d] The principal components of the chemical shift tensors are defined using the frequency-ordered convention, with $\delta_{11} \geq \delta_{22} \geq \delta_{33}$. The isotropic chemical shift, span, and skew are given by $\delta_{iso} = (\delta_{11} + \delta_{22} + \delta_{33})/3$, $\Omega = \delta_{11} - \delta_{33}$, and $\kappa = 3(\delta_{22} - \delta_{iso})/\Omega$, respectively. [e] The Euler angles α, β, and γ define the relative orientation of the EFG and chemical shift tensors using the $ZY'Z''$ convention for rotation. The experimental angles derived from ssNake (which uses the $ZX'Z''$ convention) are adjusted to match the calculated values extracted by EFGShield. [f] This parameter is not reported since has little effect on the appearance of simulated powder patterns.

parameters could be derived (Fig. 7). In contrast, the spectrum acquired at 9.4 T shows clear evidence of the narrow feature corresponding to the chloride ion Cl1, but only low signal-to-noise features with no apparent discontinuities corresponding to the broader patterns of Cl1A and Cl1B.

The local environments of chloride ions, especially number, types, and spatial arrangements of H···Cl$^-$ hydrogen bonds, influence ^{35}Cl EFG tensors, with the strongest effects exerted by those featuring r(H···Cl$^-$) of 2.2 Å or less.[44–47] Our previous work on qualitatively identifying these relationships is briefly summarized in ESI† S3. The three ^{35}Cl patterns for **pon·HCl** can be definitively assigned from DFT calculations of the ^{35}Cl chemical shift and EFG tensors on a model of the refined crystal structure (Fig. 9, Table 3). Of the three overlapping patterns evident in the ^{35}Cl spectra, the narrow pattern (C_Q = 2.21 MHz; η_Q = 0.70) corresponds to Cl1; this is one of only a handful of examples of a chloride ion in an organic crystalline solid that forms hydrogen bonds exclusively with water molecules to be characterized by ^{35}Cl SSNMR spectroscopy.[123] This site features two hydrogen bonds with water molecules at distances of r(H···Cl$^-$) = 2.234 and 2.235 Å. DFT calculations demonstrate that the sign of C_Q is positive, and V_{33} is not oriented in the direction of any hydrogen bonding axis and does not appear to be constrained by any obvious symmetry or pseudo-symmetry element. However, V_{11} and V_{22} reside approximately within the plane of the three water molecules, indicating positive EFGs within this plane and negative EFGs perpendicular to the plane. The two broader patterns correspond to chloride ions that form hydrogen bonds with both water molecules and the charged tertiary amine moieties, and have correspondingly larger magnitudes of C_Q. Cl1A (C_Q = 5.16 MHz; η_Q = 0.41) features hydrogen bonds with a charged amine moiety at r(H···Cl$^-$) = 2.151 Å and a water molecule at r(H···Cl$^-$) = 2.208 Å. Similarly, Cl1B (C_Q = 5.66 MHz; η_Q = 0.71) features hydrogen bonds with a water molecule at r(H···Cl$^-$) = 2.327 Å, a charged amine moiety at r(H···Cl$^-$) = 2.335 Å, and an amide contact at r(H···Cl$^-$) = 2.507 Å. For both sites, DFT calculations predict the sign of C_Q to be negative, with V_{33} oriented in the general direction of charged tertiary amine moiety, and approximately perpendicular to the hydrogen bond with the water molecule.

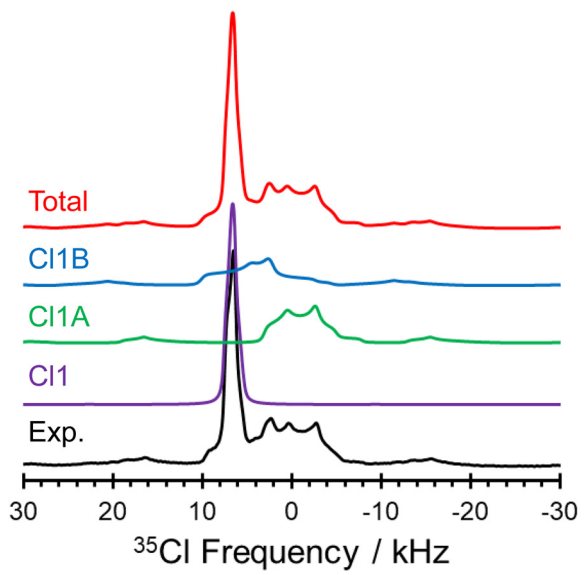

Fig. 8 Experimental ^{35}Cl spectrum of **pon·HCl** acquired at 35.2 T with a spinning rate of ν_{rot} = 16 kHz, along with a total simulated pattern representing the three overlapping chloride sites, and deconvolutions of the three underlying patterns.

In order to confirm the assignment of the chloride ions and their proximities with neighboring protons, a 2D ^{35}Cl → ^{1}H D-RINEPT spectrum was acquired with a spinning speed of ν_{rot} = 50 kHz and five rotor periods of $SR4_1^2$ recoupling (Fig. 10). Similar to the 1D ^{35}Cl MAS spectrum acquired at 35.2 T, the f_1 projection (*i.e.*, the ^{35}Cl dimension) of the 2D D-RINEPT spectrum has an overall appearance that results from three overlapping ^{35}Cl patterns, corresponding to the three crystallographically distinct chloride ions. The f_2 projection (*i.e.*, the ^{1}H dimension) features three groupings of peaks,

Open Access Article. Published on 30 January 2024. Downloaded on 2/7/2026 1:11:04 PM.
This article is licensed under a Creative Commons Attribution-NonCommercial 3.0 Unported Licence.

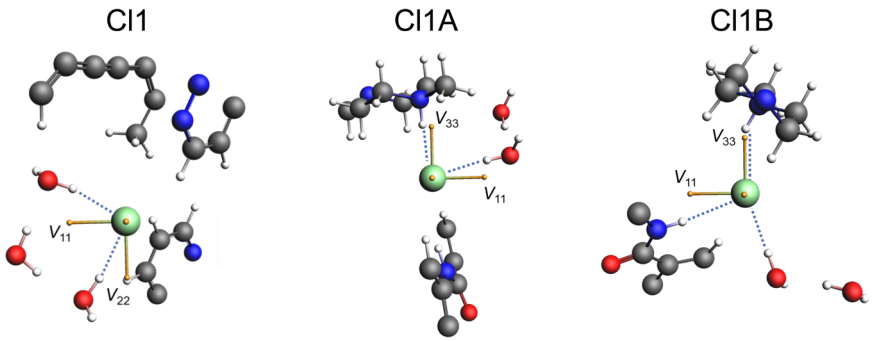

Fig. 9 ^{35}Cl EFG tensor orientations for the three chloride ions in **pon·HCl**. H···Cl$^-$ hydrogen bonds (<2.6 Å) are shown as dotted blue lines. The three yellow vectors represent the orientations of the principal components of the EFG tensors (V_{11}, V_{22}, and V_{33}), with one principal components perpendicular to the page in each case.

Table 3 Structural information for the H···Cl$^-$ hydrogen bonds in **pon·HCl**

Chloride site	Contact type[a]	H···Cl$^-$ distance[b] (Å)	X···Cl$^-$ distance[c] (Å)	X–H···Cl$^-$ angle[d] (°)
Cl1	HOH···Cl$^-$	2.234	3.142	164.4
	HOH···Cl$^-$	2.235	3.152	167.6
	CH···Cl$^-$	2.574	3.548	148.3
Cl1A	RR′R″NH$^+$···Cl$^-$	2.151	3.124	166.4
	HOH···Cl$^-$	2.208	3.122	165.9
Cl1B	HOH···Cl$^-$	2.327	3.255	177.3
	RR′R″NH$^+$···Cl$^-$	2.335	3.228	150.8
	RR′NH···Cl$^-$	2.507	3.452	166.3

[a] Indicates the functional group contributing to the H···Cl$^-$ contacts (*i.e.*, HOH···Cl$^-$ signifies a water contact, RR′R″NH$^+$···Cl$^-$ signifies a charged tertiary amine contact, and CH···Cl$^-$ signifies an aromatic contact). [b] The shortest H···Cl$^-$ hydrogen bonds (<2.6 Å, X = N, O) as determined *via* energy minimization and geometry optimization with DFT plane wave calculations. [c] Distance between the chloride ion and the hydrogen-bond donor atom (X = N, O). [d] Angle between the hydrogen-bond donor atom (X = N, O), the hydrogen atom, and the chloride atom.

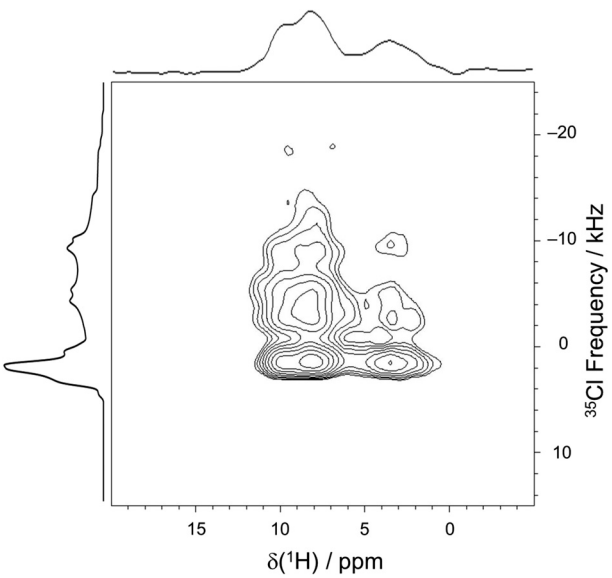

Fig. 10 2D ^{35}Cl → ^{1}H D-RINEPT correlation spectrum of **pon·HCl**, acquired at 18.8 T with ν_{rot} = 50 kHz. Five rotor periods of recoupling was found to maximize the observed signal. A 1D ^{1}H spectrum is overlaid on top of the spectrum, whereas a simulated ^{35}Cl spectrum is overlaid on the left side.

resulting in a spectrum with more detail than observed in the 1D ^{1}H MAS spectrum. The 2D D-RINEPT spectrum features several cross peaks that result from dipolar interactions between the chloride ions and nearby protons. For instance, the strong peaks that occur at $\delta_{iso}(^1H)$ = 8.5 ppm for a broad range of ^{35}Cl frequencies are indicative of interactions between Cl1A and Cl1B and the hydrogen-bond donating charged tertiary amine moieties (H6A and H6B, respectively). The cross peak at $\delta_{iso}(^1H)$ = 3.8 ppm likely corresponds to water molecules that form hydrogen bonds with each of the chloride ion sites. Finally, the peak at $\delta_{iso}(^1H)$ = 9.9 ppm, which corresponds to the aromatic proton H1AA, has a cross peak indicating correlation to Cl1; this is in accordance with the crystal structure, where r(H1AA···Cl1$^-$) = 2.507 Å.

4. Conclusion

The structure of a novel ionic cocrystal of ponatinib hydrochloride was determined by single crystal X-ray diffraction, and further characterized by SSNMR and DFT methods. The crystal structure contains both ponatinib monocations and dications, along with three chloride ions and three water molecules. The use of a variety of solid-state analytical techniques, including SCXRD and SSNMR

 This journal is © The Royal Society of Chemistry 2024

Open Access Article. Published on 30 January 2024. Downloaded on 2/7/2026 1:11:04 PM.
This article is licensed under a Creative Commons Attribution-NonCommercial 3.0 Unported Licence.

in the present case, can uncover the nature of the noncovalent bonding interactions between the API molecules and other molecular or ionic components that constitute this multicomponent crystal, providing a detailed understanding of the key hydrogen bonds that serve to stabilize the structure.

SSNMR spectroscopy is invaluable for confirming the unusual crystal structure of **pon·HCl**. 1D ^{35}Cl spectra obtained at multiple fields confirm the presence of three distinct chloride ions, which were assigned using plane-wave DFT calculations of their respective ^{35}Cl EFG and chemical shift tensors. The 2D ^{35}Cl → ^{1}H D-RINEPT spectrum confirms the spatial proximities between all three chloride ions and water molecules, amine protons, and even an aromatic proton. The ^{1}H → ^{13}C{^{1}H} CP/MAS NMR spectrum confirms the presence of two crystallographically distinct ponatinib molecules in the asymmetric unit. 1D ^{1}H and 2D ^{1}H–^{1}H DQ–SQ spectra identify an unusually deshielded ^{1}H peak, which is assigned to the imidazopyridazine moiety that forms an intermolecular hydrogen bond from the ponatinib dication to the monocation. This all suggests future applications of multinuclear SSNMR spectroscopy at high and ultra-high fields to the study of complex HCl API materials for which SCXRD data is unavailable, including those exhibiting complex ^{1}H, ^{13}C, and/or ^{35}Cl SSNMR spectra with overlapping patterns, with low wt% chlorine, and comprising heterogeneous mixtures or amorphous solid dispersions.

Conflicts of interest

There are no conflicts to declare.

Acknowledgements

The authors thank the Florida State University and the National High Magnetic Field Laboratory for funding this research (materials, computers, spectrometer time, and NMR hardware). In addition, R. W. S and S. T. H. thank the U.S. Department of Energy, Office of Science, Office of Basic Energy Sciences, under Award Number DE-SC0022310, for support of personnel involved in this work. The National High Magnetic Field Laboratory is supported by the National Science Foundation through NSF/DMR-1644779 and NSF/DMR-2128556, and the State of Florida. The Development of the 36 T Series-Connected Hybrid magnet and NMR instrumentation was supported by NSF (DMR-1039938 and DMR-0603042) and NIH (GM122698 and GM148766). The authors acknowledge the use of the MAX Diffraction Facility, McMaster University. The authors also thank the Natural Sciences and Engineering Research Council of Canada (NSERC Discovery grant 2016-06642), the Canadian Foundation for Innovation, the Ontario Innovation Trust, the Ontario Research Fund, and the University of Windsor for supporting the initial stages of this project.

References

1 S. Datta and D. J. W. Grant, Crystal structures of drugs: advances in determination, prediction and engineering, *Nat. Rev. Drug Discovery*, 2004, **3**, 42–57.
2 A. M. Healy, Z. A. Worku, D. Kumar and A. M. Madi, Pharmaceutical solvates, hydrates and amorphous forms: a special emphasis on cocrystals, *Adv. Drug Delivery Rev.*, 2017, **117**, 25–46.
3 E. Pindelska, A. Sokal and W. Kolodziejski, Pharmaceutical cocrystals, salts and polymorphs: advanced characterization techniques, *Adv. Drug Delivery Rev.*, 2017, **117**, 111–146.
4 G. P. Stahly, Diversity in single- and multiple-component crystals. the search for and prevalence of polymorphs and cocrystals, *Cryst. Growth Des.*, 2007, **7**, 1007–1026.
5 N. K. Duggirala, M. L. Perry, Ö. Almarsson and M. J. Zaworotko, Pharmaceutical cocrystals: along the path to improved medicines, *Chem. Commun.*, 2016, **52**, 640–655.
6 A. T. M. Serajuddin, Salt formation to improve drug solubility, *Adv. Drug Delivery Rev.*, 2007, **59**, 603–616.
7 S. R. Byrn, R. R. Pfeiffer, G. Stephenson, D. J. W. Grant and W. B. Gleason, Solid-state pharmaceutical chemistry, *Chem. Mater.*, 1994, **6**, 1148–1158.
8 D. E. Bugay, Characterization of the solid-state: spectroscopic techniques, *Adv. Drug Delivery Rev.*, 2001, **48**, 43–65.
9 S. L. Childs, G. P. Stahly and A. Park, The salt–cocrystal continuum: the influence of crystal structure on ionization state, *Mol. Pharmaceutics*, 2007, **4**, 323–338.
10 P. Stainton, E. Nauha, T. Grecu, J. F. McCabe, T. Munshi, I. Scowen, H. C. S. Chan, S. Nilsson and N. Blagden, Chameleon behavior of a new salt of 3-(aminocarbonyl) pyridinium malonate and implications for polymorphism on the salt/cocrystal continuum, *Cryst. Growth Des.*, 2022, **22**, 1665–1679.
11 A. O. F. Jones, N. Blagden, G. J. McIntyre, A. Parkin, C. C. Seaton, L. H. Thomas and C. C. Wilson, Tuning proton disorder in 3,5-dinitrobenzoic acid dimers: the effect of local environment, *Cryst. Growth Des.*, 2013, **13**, 497–509.
12 S. Aitipamula, R. Banerjee, A. K. Bansal, K. Biradha, M. L. Cheney, A. R. Choudhury, G. R. Desiraju, A. G. Dikundwar, R. Dubey and N. Duggirala, *et al.*, Polymorphs, salts, and cocrystals: what's in a name?, *Cryst. Growth Des.*, 2012, **12**, 2147–2152.
13 W. T. A. Harrison, H. S. Yathirajan, S. Bindya, H. G. Anilkumar and Devaraju, Escitalopram oxalate: co-existence of oxalate dianions and oxalic acid molecules in the same crystal, *Acta Crystallogr., Sect. C: Cryst. Struct. Commun.*, 2007, **63**, o129–o131.
14 C. Wang, T. D. Turner, C. Y. Ma, C. M. Pask, I. Rosbottom, R. S. Hong, A. Y. Sheikh, Q. Yin and K. J. Roberts, A quaternary solid-form of ritonavir: an oxalate salt oxalic acid co-crystal acetone solvate, *CrystEngComm*, 2023, **25**, 1782–1791.
15 M. Pop, P. Sieger and P. W. Cains, Tiotropium fumarate: an interesting pharmaceutical co-crystal, *J. Pharm. Sci.*, 2009, **98**, 1820–1834.

Open Access Article. Published on 30 January 2024. Downloaded on 2/7/2026 1:11:04 PM.
This article is licensed under a Creative Commons Attribution-NonCommercial 3.0 Unported Licence.

16 M. Li, W. Xu and Y. Su, Solid-state NMR spectroscopy in pharmaceutical sciences, *TrAC, Trends Anal. Chem.*, 2021, **135**, 116152.
17 R. K. Harris, NMR studies of organic polymorphs & solvates, *Analyst*, 2006, **131**, 351–373.
18 R. T. Berendt, D. M. Sperger, E. J. Munson and P. K. Isbester, Solid-state NMR spectroscopy in pharmaceutical research and analysis, *TrAC, Trends Anal. Chem.*, 2006, **25**, 977–984.
19 M. Geppi, G. Mollica, S. Borsacchi and C. A. Veracini, Solid-state NMR studies of pharmaceutical systems, *Appl. Spectrosc. Rev.*, 2008, **43**, 202–302.
20 F. G. Vogt, Evolution of solid-state NMR in pharmaceutical analysis, *Future Med. Chem.*, 2010, **2**, 915–921.
21 F. G. Vogt, Solid-State NMR in Drug Discovery and Development, in *New Applications of NMR in Drug Discovery and Development*, The Royal Society of Chemistry, 2013, pp. 43–100.
22 D. Massiot, F. Fayon, M. Capron, I. King, S. Le Calvé, B. Alonso, J.-O. Durand, B. Bujoli, Z. Gan and G. Hoatson, Modelling one- and two-dimensional solid-state NMR spectra, *Magn. Reson. Chem.*, 2002, **40**, 70–76.
23 J. K. Harper and D. M. Grant, Enhancing crystal-structure prediction with NMR tensor data, *Cryst. Growth Des.*, 2006, **6**, 2315–2321.
24 J. K. Harper, J. A. Doebbler, E. Jacques, D. M. Grant and R. B. Von Dreele, A combined solid-state NMR and synchrotron X-ray diffraction powder study on the structure of the antioxidant (+)-catechin 4.5-hydrate, *J. Am. Chem. Soc.*, 2010, **132**, 2928–2937.
25 J. K. Harper, D. M. Grant, Y. Zhang, P. L. Lee and R. Von Dreele, Characterizing challenging microcrystalline solids with solid-state NMR shift tensor and synchrotron X-ray powder diffraction data: structural analysis of ambuic acid, *J. Am. Chem. Soc.*, 2006, **128**, 1547–1552.
26 J. K. Harper, D. H. Barich, E. M. Heider, D. M. Grant, R. R. Franke, J. H. Johnson, Y. Zhang, P. L. Lee, R. B. Von Dreele and B. Scott, *et al.*, A combined solid-state NMR and X-ray powder diffraction study of a stable polymorph of paclitaxel, *Cryst. Growth Des.*, 2005, **5**, 1737–1742.
27 C. J. H. Smalley, H. E. Hoskyns, C. E. Hughes, D. N. Johnstone, T. Willhammar, M. T. Young, C. J. Pickard, A. J. Logsdail, P. A. Midgley and K. D. M. Harris, A structure determination protocol based on combined analysis of 3D-ED data, powder XRD data, solid-state NMR data and DFT-D calculations reveals the structure of a new polymorph of l-tyrosine, *Chem. Sci.*, 2022, **13**, 5277–5288.
28 C. E. Hughes, G. N. M. Reddy, S. Masiero, S. P. Brown, P. A. Williams and K. D. M. Harris, Determination of a complex crystal structure in the absence of single crystals: analysis of powder X-ray diffraction data, guided by solid-state NMR and periodic DFT calculations, reveals a new 2′-deoxyguanosine structural motif, *Chem. Sci.*, 2017, **8**, 3971–3979.
29 A. E. Watts, K. Maruyoshi, C. E. Hughes, S. P. Brown and K. D. M. Harris, Combining the advantages of powder X-ray diffraction and NMR crystallography in structure determination of the pharmaceutical material cimetidine hydrochloride, *Cryst. Growth Des.*, 2016, **16**, 1798–1804.
30 E. Salager, R. S. Stein, C. J. Pickard, B. Elena and L. Emsley, Powder NMR crystallography of thymol, *Phys. Chem. Chem. Phys.*, 2009, **11**, 2610–2621.
31 E. Salager, G. M. Day, R. S. Stein, C. J. Pickard, B. Elena and L. Emsley, Powder crystallography by combined crystal structure prediction and high-resolution ^{1}H solid-state NMR spectroscopy, *J. Am. Chem. Soc.*, 2010, **132**, 2564–2566.
32 M. Baias, J.-N. Dumez, P. H. Svensson, S. Schantz, G. M. Day and L. Emsley, De novo determination of the crystal structure of a large drug molecule by crystal structure prediction-based powder NMR crystallography, *J. Am. Chem. Soc.*, 2013, **135**, 17501–17507.
33 E. A. Engel, A. Anelli, A. Hofstetter, F. Paruzzo, L. Emsley and M. Ceriotti, A Bayesian approach to NMR crystal structure determination, *Phys. Chem. Chem. Phys.*, 2019, **21**, 23385–23400.
34 M. Balodis, M. Cordova, A. Hofstetter, G. M. Day and L. Emsley, De novo crystal structure determination from machine learned chemical shifts, *J. Am. Chem. Soc.*, 2022, **144**, 7215–7223.
35 A. S. Tatton, H. Blade, S. P. Brown, P. Hodgkinson, L. P. Hughes, S. O. N. Lill and J. R. Yates, Improving confidence in crystal structure solutions using NMR crystallography: the case of β-piroxicam, *Cryst. Growth Des.*, 2018, **18**, 3339–3351.
36 S. T. Holmes, W. D. Wang, G. Hou, C. Dybowski, W. Wang and S. Bai, A new NMR crystallographic approach to reveal the calcium local structure of atorvastatin calcium, *Phys. Chem. Chem. Phys.*, 2019, **21**, 6319–6326.
37 N. Variankaval, R. Wenslow, J. Murry, R. Hartman, R. Helmy, E. Kwong, S.-D. Clas, C. Dalton and I. Santos, Preparation and solid-state characterization of nonstoichiometric cocrystals of a phosphodiesterase-IV inhibitor and L-tartaric acid, *Cryst. Growth Des.*, 2006, **6**, 690–700.
38 S. T. Holmes, O. G. Engl, M. N. Srnec, J. D. Madura, R. Quiñones, J. K. Harper, R. W. Schurko and R. J. Iuliucci, Chemical shift tensors of cimetidine form A modeled with density functional theory calculations: implications for NMR crystallography, *J. Phys. Chem. A*, 2020, **124**, 3109–3119.
39 M. Dudek, P. Paluch and E. Pindelska, Crystal structures of two furazidin polymorphs revealed by a joint effort of crystal structure prediction and NMR crystallography, *Acta Crystallogr., Sect. B: Struct. Sci., Cryst. Eng. Mater.*, 2020, **76**, 322–335.
40 W. D. Wang, X. Gao, M. Strohmeier, W. Wang, S. Bai and C. Dybowski, Solid-state NMR studies of form I of atorvastatin calcium, *J. Phys. Chem. B*, 2012, **116**, 3641–3649.
41 J. K. Harper, R. Iuliucci, M. Gruber and K. Kalakewich, Refining crystal structures with experimental ^{13}C NMR shift tensors and lattice-including electronic structure methods, *CrystEngComm*, 2013, **15**, 8693–8704.

 This journal is © The Royal Society of Chemistry 2024

Open Access Article. Published on 30 January 2024. Downloaded on 2/7/2026 1:11:04 PM.
This article is licensed under a Creative Commons Attribution-NonCommercial 3.0 Unported Licence.

42 S. P. Brown, Applications of high-resolution ^{1}H solid-state NMR, *Solid State Nucl. Magn. Reson.*, 2012, **41**, 1–27.
43 G. S. Paulekuhn, J. B. Dressman and C. Saal, Trends in active pharmaceutical ingredient salt selection based on analysis of the orange book database, *J. Med. Chem.*, 2007, **50**, 6665–6672.
44 H. Hamaed, J. M. Pawlowski, B. F. T. Cooper, R. Fu, S. H. Eichhorn and R. W. Schurko, Application of solid-state ^{35}Cl NMR to the structural characterization of hydrochloride pharmaceuticals and their polymorphs, *J. Am. Chem. Soc.*, 2008, **130**, 11056–11065.
45 M. Hildebrand, H. Hamaed, A. M. Namespetra, J. M. Donohue, R. Fu, I. Hung, Z. Gan and R. W. Schurko, ^{35}Cl solid-state NMR of HCl salts of active pharmaceutical ingredients: structural prediction, spectral fingerprinting and polymorph recognition, *CrystEngComm*, 2014, **16**, 7334–7356.
46 S. T. Holmes, J. M. Hook and R. W. Schurko, Nutraceuticals in bulk and dosage forms: analysis by ^{35}Cl and ^{14}N solid-state NMR and DFT calculations, *Mol. Pharmaceutics*, 2022, **19**, 440–455.
47 A. A. Peach, D. A. Hirsh, S. T. Holmes and R. W. Schurko, Mechanochemical syntheses and ^{35}Cl solid-state NMR characterization of fluoxetine HCl cocrystals, *CrystEngComm*, 2018, **20**, 2780–2792.
48 A. M. Namespetra, D. A. Hirsh, M. P. Hildebrand, A. R. Sandre, H. Hamaed, J. M. Rawson and R. W. Schurko, ^{35}Cl solid-state NMR spectroscopy of HCl pharmaceuticals and their polymorphs in bulk and dosage forms, *CrystEngComm*, 2016, **18**, 6213–6232.
49 S. T. Holmes, C. S. Vojvodin, N. Veinberg, E. M. Iacobelli, D. A. Hirsh and R. W. Schurko, Hydrates of active pharmaceutical ingredients: A ^{35}Cl and ^{2}H solid-state NMR and DFT study, *Solid State Nucl. Magn. Reson.*, 2022, **122**, 101837.
50 A. A. Peach, S. T. Holmes, L. R. MacGillivray and R. W. Schurko, The formation and stability of fluoxetine HCl cocrystals investigated by multicomponent milling, *CrystEngComm*, 2023, **25**, 213–224.
51 D. A. Hirsh, A. J. Rossini, L. Emsley and R. W. Schurko, ^{35}Cl dynamic nuclear polarization solid-state NMR of active pharmaceutical ingredients, *Phys. Chem. Chem. Phys.*, 2016, **18**, 25893–25904.
52 L. M. Abdulla, A. A. Peach, S. T. Holmes, Z. T. Dowdell, L. K. Watanabe, E. M. Iacobelli, D. A. Hirsh, J. M. Rawson and R. W. Schurko, Synthesis and characterization of xylazine hydrochloride polymorphs, hydrates, and focrystals: a ^{35}Cl solid-state NMR and DFT study, *Cryst. Growth Des.*, 2023, **23**, 3412–3426.
53 C. S. Vojvodin, S. T. Holmes, L. K. Watanabe, J. M. Rawson and R. W. Schurko, Multi-component crystals containing urea: mechanochemical synthesis and characterization by ^{35}Cl solid-state NMR spectroscopy and DFT calculations, *CrystEngComm*, 2022, **24**, 2626–2641.
54 F. G. Vogt, G. R. Williams, M. Strohmeier, M. N. Johnson and R. C. B. Copley, Solid-state NMR analysis of a complex crystalline phase of ronacaleret hydrochloride, *J. Phys. Chem. B*, 2014, **118**, 10266–10284.
55 F. G. Vogt, G. R. Williams and R. C. B. Copley, Solid-state NMR analysis of a boron-containing pharmaceutical hydrochloride salt, *J. Pharm. Sci.*, 2013, **102**, 3705–3716.
56 D. A. Hirsh, Y. Su, H. Nie, W. Xu, D. Stueber, N. Variankaval and R. W. Schurko, Quantifying disproportionation in pharmaceutical formulations with ^{35}Cl solid-state NMR, *Mol. Pharmaceutics*, 2018, **15**, 4038–4048.
57 D. A. Hirsh, S. T. Holmes, P. Chakravarty, A. A. Peach, A. G. DiPasquale, K. Nagapudi and R. W. Schurko, In situ characterization of waters of hydration in a variable-hydrate active pharmaceutical ingredient using ^{35}Cl solid-state NMR and X-ray diffraction, *Cryst. Growth Des.*, 2019, **19**, 7349–7362.
58 P. M. J. Szell, Z. Rehman, B. P. Tatman, L. P. Hughes, H. Blade and S. P. Brown, Exploring the potential of multinuclear solid-state ^{1}H, ^{13}C, and ^{35}Cl magnetic resonance to characterize static and dynamic disorder in pharmaceutical hydrochlorides, *ChemPhysChem*, 2023, **24**, e202200946.
59 M. K. Pandey, H. Kato, Y. Ishii and Y. Nishiyama, Two-dimensional proton-detected ^{35}Cl/^{1}H correlation solid-state NMR experiment under fast magic angle sample spinning: application to pharmaceutical compounds, *Phys. Chem. Chem. Phys.*, 2016, **18**, 6209–6216.
60 A. Venkatesh, M. P. Hanrahan and A. J. Rossini, Proton detection of MAS solid-state NMR spectra of half-integer quadrupolar nuclei, *Solid State Nucl. Magn. Reson.*, 2017, **84**, 171–181.
61 A. V. Wijesekara, A. Venkatesh, B. J. Lampkin, B. VanVeller, J. W. Lubach, K. Nagapudi, I. Hung, P. L. Gor'kov, Z. Gan and A. J. Rossini, Fast acquisition of proton-detected HETCOR solid-state NMR spectra of quadrupolar nuclei and rapid measurement of NH bond lengths by frequency selective HMQC and RESPDOR pulse sequences, *Chem. – Eur. J.*, 2020, **26**, 7881–7888.
62 D. Iuga, E. K. Corlett and S. P. Brown, ^{35}Cl-^{1}H heteronuclear correlation MAS NMR experiments for probing pharmaceutical salts, *Magn. Reson. Chem.*, 2021, **59**, 1089–1100.
63 I. Hung and Z. Gan, Satellite-transition double cross-polarization HETCOR under fast MAS, *J. Magn. Reson.*, 2023, **348**, 107380.
64 L. Frydman and J. S. Harwood, Isotropic spectra of half-integer quadrupolar spins from bidimensional magic-angle spinning NMR, *J. Am. Chem. Soc.*, 1995, **117**, 5367–5368.
65 A. Medek, J. S. Harwood and L. Frydman, Multiple-quantum magic-angle spinning NMR: a new method for the study of quadrupolar nuclei in solids, *J. Am. Chem. Soc.*, 1995, **117**, 12779–12787.
66 I. Hung and Z. Gan, Pushing the limit of MQMAS for low-γ quadrupolar nuclei in pharmaceutical hydrochlorides, *J. Magn. Reson.*, 2023, 107423.
67 W.-S. Huang, C. A. Metcalf, R. Sundaramoorthi, Y. Wang, D. Zou, R. M. Thomas, X. Zhu, L. Cai, D. Wen and S. Liu,

Open Access Article. Published on 30 January 2024. Downloaded on 2/7/2026 1:11:04 PM. This article is licensed under a Creative Commons Attribution-NonCommercial 3.0 Unported Licence.

et al., Discovery of 3-[2-(omidazo[1,2-b]pyridazin-3-yl) ethynyl]-4-methyl-N-{4-[(4-methylpiperazin-1-yl)methyl]-3-(trifluoromethyl)phenyl}benzamide (AP24534), a potent, orally active pan-inhibitor of breakpoint cluster region-Abelson (BCR-ABL) kinase including the T315I gatekeeper mutant, *J. Med. Chem.*, 2010, **53**, 4701–4719.

68 T. O'Hare, W. C. Shakespeare, X. Zhu, C. A. Eide, V. M. Rivera, F. Wang, L. T. Adrian, T. Zhou, W.-S. Huang and Q. Xu, *et al.*, AP24534, a pan-BCR-ABL inhibitor for chronic myeloid leukemia, potently inhibits the T315I mutant and overcomes mutation-based resistance, *Cancer Cell*, 2009, **16**, 401–412.

69 M. Stefinovic, H. Reece and A. Sunkara, Crystalline forms of ponatinib hydrochloride, WO/2015/001098, 2015.

70 C. K. Murray, L. W. Rozamus, J. J. Chaber and P. Sharma, Crystalline forms of 3-(imidazo[1,2-B] pyridazin-3-ylethynyl)-4-methyl-N-{4-[(4-methylpiperazin-1-yl) methyl]-3-(trifluoromethyl)phenyl}benzamide and its mono hydrochloride salt, WO/2014/093579, 2014.

71 V. Kiss, E. Tieger, L. Ridvan, M. Tkadlecova, O. Dammer and L. Krejcik, Modification of 3-(imidazo[1,2-B] pyridazin-3-ylethynyl)-4-methyl-N-(4-[(4-methylpiperazin-1-yl) methyl]-3-(trifluoromethyl)phenyl) benzamide hydrochloride salt, WO/2015/085973, 2015.

72 J. H. Lipton, C. Chuah, A. Guerci-Bresler, G. Rosti, D. Simpson, S. Assouline, G. Etienne, F. E. Nicolini, P. le Coutre and R. E. Clark, *et al.*, Ponatinib versus imatinib for newly diagnosed chronic myeloid leukaemia: an international, randomised, open-label, phase 3 trial, *Lancet*, 2016, **17**, P612–P621.

73 F. H. Tan, T. L. Putoczki, S. S. Stylli and R. B. Luwor, Ponatinib: a novel multi-tyrosine kinase inhibitor against human malignancies, *OncoTargets Ther.*, 2019, **12**, 635–645.

74 Experts in Chronic Myeloid Leukemia, The price of drugs for chronic myeloid leukemia (CML) is a reflection of the unsustainable prices of cancer drugs: from the perspective of a large group of CML experts, *Blood*, 2013, **121**, 4439–4442.

75 F. E. S. Souza, B. Khalili, K. A. Rantanen, J. L. Gerster, A. Bhattacharyya, B. Gorin and A. W. Rey, Crystalline forms of ponatinib hydrochloride, US11072620B2, 2018.

76 O. V. Dolomanov, L. J. Bourhis, R. J. Gildea, J. A. K. Howard and H. Puschmann, OLEX2: a complete structure solution, refinement and analysis program, *J. Appl. Crystallogr.*, 2009, **42**, 339–341.

77 G. M. Sheldrick, SHELXT - integrated space-group and crystal-structure determination, *Acta Crystallogr., Sect. A: Found. Adv.*, 2015, **71**, 3–8.

78 G. M. Sheldrick, A short history of SHELX, *Acta Crystallogr., Sect. A: Found. Crystallogr.*, 2008, **64**, 112–122.

79 Z. Gan, I. Hung, X. Wang, J. Paulino, G. Wu, I. M. Litvak, P. L. Gor'kov, W. W. Brey, P. Lendi and J. L. Schiano, *et al.*, NMR spectroscopy up to 35.2 T using a series-connected hybrid magnet, *J. Magn. Reson.*, 2017, **284**, 125–136.

80 S. G. J. van Meerten, W. M. J. Franssen and A. P. M. Kentgens, ssNake: a cross-platform open-source NMR data processing and fitting application, *J. Magn. Reson.*, 2019, **301**, 56–66.

81 A. Pines, J. S. Waugh and M. G. Gibby, Proton-enhanced nuclear induction spectroscopy. ^{13}C chemical shielding anisotropy in some organic solids, *Chem. Phys. Lett.*, 1972, **15**, 373–376.

82 J. Schaefer and E. O. Stejskal, Carbon-13 nuclear magnetic resonance of polymers spinning at the magic angle, *J. Am. Chem. Soc.*, 1976, **98**, 1031–1032.

83 O. B. Peersen, X. L. Wu, I. Kustanovich and S. O. Smith, Variable-amplitude cross-polarization MAS NMR, *J. Magn. Reson., Ser. A*, 1993, **104**, 334–339.

84 G. Metz, X. L. Wu and S. O. Smith, Ramped-amplitude pross Polarization in magic-angle-spinning NMR, *J. Magn. Reson., Ser. A*, 1994, **110**, 219–227.

85 B. M. Fung, A. K. Khitrin and K. Ermolaev, An improved broadband decoupling sequence for liquid crystals and solids, *J. Magn. Reson.*, 2000, **142**, 97–101.

86 S. R. Hartmann and E. L. Hahn, Nuclear double resonance in the rotating frame, *Phys. Rev.*, 1962, **128**, 2042–2053.

87 R. E. Taylor, Setting up ^{13}C CP/MAS experiments, *Concepts Magn. Reson., Part A*, 2004, **22**, 37–49.

88 W. Sommer, J. Gottwald, D. E. Demco and H. W. Spiess, Dipolar heteronuclear multiple-quantum NMR spectroscopy in rotating solids, *J. Magn. Reson.*, 1995, **113**, 131–134.

89 I. Schnell, A. Lupulescu, S. Hafner, D. E. Demco and H. W. Spiess, Resolution enhancement in multiple-quantum MAS NMR spectroscopy, *J. Magn. Reson.*, 1998, **133**, 61–69.

90 J. Trebosc, B. Hu, J. P. Amoureux and Z. Gan, Through-space R^3-HETCOR experiments between spin-1/2 and half-integer quadrupolar nuclei in solid-state NMR, *J. Magn. Reson.*, 2007, **186**, 220–227.

91 A. Brinkmann and A. P. M. Kentgens, Proton-selective ^{17}O–^{1}H distance measurements in fast magic-angle-spinning solid-state NMR spectroscopy for the determination of hydrogen bond lengths, *J. Am. Chem. Soc.*, 2006, **128**, 14758–14759.

92 Z. Gan, Rotary resonance echo double resonance for measuring heteronuclear dipolar coupling under MAS, *J. Magn. Reson.*, 2006, **183**, 235–241.

93 M. Goswami and P. K. Madhu, Sensitivity enhancement of the central-transition signal of half-integer spin quadrupolar nuclei in solid-state NMR: Features of multiple fast amplitude-modulated pulse transfer, *J. Magn. Reson.*, 2008, **192**, 230–234.

94 H.-T. Kwak, S. Prasad, T. Clark and P. J. Grandinetti, Enhancing sensitivity of quadrupolar nuclei in solid-state NMR with multiple rotor assisted population transfers, *Solid State Nucl. Magn. Reson.*, 2003, **24**, 71–77.

95 S. J. Clark, M. D. Segall, C. J. Pickard, P. J. Hasnip, M. J. Probert, K. Refson and M. C. Payne, First principles methods using CASTEP, *Z. Kristallogr.*, 2005, **220**, 567–570.

96 B. Hammer, L. B. Hansen and J. K. Nørskov, Improved adsorption energetics within density-functional theory using revised Perdew-Burke-Ernzerhof functionals, *Phys. Rev. B: Condens. Matter Mater. Phys.*, 1999, **59**, 7413–7421.

 This journal is © The Royal Society of Chemistry 2024

Open Access Article. Published on 30 January 2024. Downloaded on 2/7/2026 1:11:04 PM.
This article is licensed under a Creative Commons Attribution-NonCommercial 3.0 Unported Licence.

97 J. R. Yates, C. J. Pickard and F. Mauri, Calculation of NMR chemical shifts for extended systems using ultrasoft pseudopotentials, *Phys. Rev. B*, 2007, **76**, 024401.
98 H. J. Monkhorst and J. D. Pack, Special points for Brillouin-zone integrations, *Phys. Rev. B*, 1976, **13**, 5188–5192.
99 B. G. Pfrommer, M. Côté, S. G. Louie and M. L. Cohen, Relaxation of crystals with the quasi-Newton method, *J. Comput. Phys.*, 1997, **131**, 233–240.
100 S. Grimme, Semiempirical GGA-type density functional constructed with a long-range dispersion correction, *J. Comput. Chem.*, 2006, **27**, 1787–1799.
101 E. R. McNellis, J. Meyer and K. Reuter, Azobenzene at coinage metal surfaces: role of dispersive van der Waals interactions, *Phys. Rev. B*, 2009, **80**, 205414.
102 S. T. Holmes, R. J. Iuliucci, K. T. Mueller and C. Dybowski, Semi-empirical refinements of crystal structures using ^{17}O quadrupolar-coupling tensors, *J. Chem. Phys.*, 2017, **146**, 064201.
103 S. T. Holmes and R. W. Schurko, Refining crystal structures with quadrupolar NMR and dispersion-corrected density functional theory, *J. Phys. Chem. C*, 2018, **122**, 1809–1820.
104 S. T. Holmes, C. S. Vojvodin and R. W. Schurko, Dispersion-corrected DFT methods for applications in nuclear magnetic resonance crystallography, *J. Phys. Chem. A*, 2020, **124**, 10312–10323.
105 J.-D. Chai and S.-P. Mao, Seeking for reliable double-hybrid density functionals without fitting parameters: The PBE0-2 functional, *Chem. Phys. Lett.*, 2012, **538**, 121–125.
106 S. Grimme, S. Ehrlich and L. Goerigk, Effect of the damping function in dispersion corrected density functional theory, *J. Comput. Chem.*, 2011, **32**, 1456–1465.
107 L. Goerigk and S. Grimme, Double-hybrid density functionals, *WIREs Comput. Mol. Sci.*, 2014, **4**, 576–600.
108 A. D. Becke, A multicenter numerical integration scheme for polyatomic molecules, *J. Chem. Phys.*, 1988, **88**, 2547–2553.
109 M. Franchini, P. H. T. Philipsen and L. Visscher, The Becke fuzzy cells integration scheme in the Amsterdam Density Functional program suite, *J. Comput. Chem.*, 2013, **34**, 1819–1827.
110 C. J. Pickard and F. Mauri, All-electron magnetic response with pseudopotentials: NMR chemical shifts, *Phys. Rev. B*, 2001, **63**, 245101.
111 R. Ditchfield, Self-consistent perturbation theory of diamagnetism, *Mol. Phys.*, 1974, **27**, 789–807.
112 K. Wolinski, J. F. Hinton and P. Pulay, Efficient implementation of the gauge-independent atomic orbital method for NMR chemical shift calculations, *J. Am. Chem. Soc.*, 1990, **112**, 8251–8260.
113 A. Rodriguez-Fortea, P. Alemany and T. Ziegler, Density functional calculations of NMR chemical chifts with the inclusion of spin–orbit coupling in tungsten and lead compounds, *J. Phys. Chem. A*, 1999, **103**, 8288–8294.
114 M. Krykunov, T. Ziegler and E. van Lenthe, Implementation of a hybrid DFT method for calculating NMR shieldings using Slater-type orbitals with spin –orbital coupling included. applications to ^{187}Os, ^{195}Pt, and ^{13}C in geavy-metal complexes, *J. Phys. Chem. A*, 2009, **113**, 11495–11500.
115 M. Krykunov, T. Ziegler and E. V. Lenthe, Hybrid density functional calculations of nuclear magnetic shieldings using Slater-type orbitals and the zeroth-order regular approximation, *Int. J. Quantum Chem.*, 2009, **109**, 1676–1683.
116 C. Adamo and V. Barone, Toward reliable density functional methods without adjustable parameters: The PBE0 model, *J. Chem. Phys.*, 1999, **110**, 6158–6170.
117 P. Moutzouri, B. Simões de Almeida, D. Torodii and L. Emsley, Pure isotropic proton solid state NMR, *J. Am. Chem. Soc.*, 2021, **143**, 9834–9841.
118 M. Strohmeier, D. Stueber and D. M. Grant, Accurate ^{13}C and ^{15}N chemical shift and ^{14}N quadrupolar coupling constant calculations in amino acid crystals: zwitterionic, hydrogen-bonded systems, *J. Phys. Chem. A*, 2003, **107**, 7629–7642.
119 O. Socha, P. Hodgkinson, C. M. Widdifield, J. R. Yates and M. Dracinsky, Exploring systematic discrepancies in DFT calculations of chlorine nuclear quadrupole couplings, *J. Phys. Chem. A*, 2017, 4103–4113.
120 I. Lopes, L. Piao, L. Stievano and J.-F. Lambert, Adsorption of amino acids on oxide supports: a solid-state NMR study of glycine adsorption on silica and alumina, *J. Phys. Chem. C*, 2009, **113**, 18163–18172.
121 S. Adiga, D. Aebi and D. L. Bryce, EFGShield — a program for parsing and summarizing the results of electric field gradient and nuclear magnetic shielding tensor calculations, *Can. J. Chem.*, 2007, **85**, 496–505.
122 B. Elena, G. Pintacuda, N. Mifsud and L. Emsley, Molecular structure determination in powders by NMR crystallography from proton spin diffusion, *J. Am. Chem. Soc.*, 2006, **128**, 9555–9560.
123 D. A. Safin, P. M. J. Szell, A. Keller, I. Korobkov, D. L. Bryce and M. Murugesu, Interaction of 2,4,6-tris(2-pyrimidyl)-1,3,5-triazine (TPymT) with CoX_2 (X = Cl, Br) in water: trapping of new self-assembled water–chloride/bromide clusters in a $[Co(bpca)_2]^+$ host (bpca = bis(2-pyrimidylcarbonyl)amidate anion), *New J. Chem.*, 2015, **39**, 7147–7152.